IOP Publishing | Institute of Physics and Engineering in Medicine Physics in Medicine & Biology

Phys. Med. Biol. **61** (2016) 6531–6552 doi:10.1088/0031-9155/61/17/6531

Atlas-guided generation of pseudo-CT images for MRI-only and hybrid PET–MRI-guided radiotherapy treatment planning

Hossein Arabi[1], Nikolaos Koutsouvelis[2], Michel Rouzaud[2], Raymond Miralbell[2] and Habib Zaidi[1,3,4,5]

[1] Division of Nuclear Medicine and Molecular Imaging, Geneva University Hospital, Geneva, CH-1211, Switzerland
[2] Division of Radiation Oncology, Geneva University Hospital, Geneva, Switzerland
[3] Geneva Neuroscience Centre, University of Geneva, Geneva, Switzerland
[4] Department of Nuclear Medicine and Molecular Imaging, University of Groningen, Groningen, Netherlands
[5] Department of Nuclear Medicine, University of Southern Denmark, DK-500, Odense, Denmark

E-mail: habib.zaidi@hcuge.ch

Received 18 December 2015, revised 13 July 2016
Accepted for publication 22 July 2016
Published 16 August 2016

Abstract

Magnetic resonance imaging (MRI)-guided attenuation correction (AC) of positron emission tomography (PET) data and/or radiation therapy (RT) treatment planning is challenged by the lack of a direct link between MRI voxel intensities and electron density. Therefore, even if this is not a trivial task, a pseudo-computed tomography (CT) image must be predicted from MRI alone. In this work, we propose a two-step (segmentation and fusion) atlas-based algorithm focusing on bone tissue identification to create a pseudo-CT image from conventional MRI sequences and evaluate its performance against the conventional MRI segmentation technique and a recently proposed multi-atlas approach. The clinical studies consisted of pelvic CT, PET and MRI scans of 12 patients with loco-regionally advanced rectal disease. In the first step, bone segmentation of the target image is optimized through local weighted atlas voting. The obtained bone map is then used to assess the quality of deformed atlases to perform voxel-wise weighted atlas fusion. To evaluate the performance of the method, a leave-one-out cross-validation (LOOCV) scheme was devised to find optimal parameters for the model. Geometric evaluation of the produced pseudo-CT images and quantitative analysis of the accuracy of PET AC were performed. Moreover, a dosimetric evaluation of volumetric modulated arc therapy photon treatment plans calculated using the different pseudo-CT images was carried out and compared to those produced

using CT images serving as references. The pseudo-CT images produced using the proposed method exhibit bone identification accuracy of 0.89 based on the Dice similarity metric compared to 0.75 achieved by the other atlas-based method. The superior bone extraction resulted in a mean standard uptake value bias of $-1.5 \pm 5.0\%$ (mean $\pm$ SD) in bony structures compared to $-19.9 \pm 11.8\%$ and $-8.1 \pm 8.2\%$ achieved by MRI segmentation-based (water-only) and atlas-guided AC. Dosimetric evaluation using dose volume histograms and the average difference between minimum/maximum absorbed doses revealed a mean error of less than 1% for the both target volumes and organs at risk. Two-dimensional (2D) gamma analysis of the isocenter dose distributions at 1%/1 mm criterion revealed pass rates of $91.40 \pm 7.56\%$, $96.00 \pm 4.11\%$ and $97.67 \pm 3.6\%$ for MRI segmentation, atlas-guided and the proposed methods, respectively. The proposed method generates accurate pseudo-CT images from conventional Dixon MRI sequences with improved bone extraction accuracy. The approach is promising for potential use in PET AC and MRI-only or hybrid PET/MRI-guided RT treatment planning.

Keywords: PET/MRI, attenuation correction, atlas-based segmentation, pseudo-CT, radiation therapy, treatment planning

(Some figures may appear in colour only in the online journal)

1. Introduction

Magnetic resonance imaging (MRI) is increasingly being used and is becoming the modality of choice in radiation therapy (RT) treatment planning of a number of clinical indications (Schmidt and Payne 2015). Likewise, positron emission tomography (PET) provides valuable complimentary information to the RT process, especially when combined with computed tomography (CT) using hybrid PET/CT scanners. In PET imaging, correcting for photon attenuation, which is commonly performed using CT, is essential for accurate quantification of tracer uptake and improved lesion detectability. The primary merit of MRI is its capability of providing superior soft tissue contrast, which leads to the reliable identification of malignancies and precise delineation of target volumes and organs at risk (OAR) compared to CT (Rasch *et al* 2005, Prabhakar *et al* 2007, Ahmed *et al* 2010). The organs delineated on MRI should be copied on CT images and as such, the two images must be spatially aligned. Manual and/or automated rigid registration between the MRI and CT scans is commonly used in the clinic. However, a mean registration error of approximately 2 mm can be expected in this process for body sites such as the prostate, which results in a systematic shift in organ contours and may ultimately lead to target under or over-dosage or excessive dose delivery to neighbouring organs (Cattaneo *et al* 2005, Nyholm *et al* 2009, Ulin *et al* 2010). RT treatment planning based solely on MRI provides a number of advantages (Brunt 2010, Schmidt and Payne 2015); however, excluding CT from the RT chain is not trivial since the MRI signal is correlated to proton density and magnetic relaxation properties, not to electron density and linear attenuation coefficients (LACs) of tissues (Mehranian *et al* 2016). In addition, conventional MRI sequences contain no signal or else a very weak signal from cortical bone which makes patient setup using digitally reconstructed radiographs (DRRs) practically unfeasible. Since both the patient and the treatment machine are virtual, the simulation film or DRR is a reconstructed image which resembles a standard two-dimensional (2D) simulation radiograph but which is

in practice generated from CT images. The lack of a separate bone tissue class or inaccurate bone delineation in the attenuation map (μ-map) has been shown to result in a substantial PET quantification bias (Andersen *et al* 2014, Dickson *et al* 2014) and dose calculation inaccuracy (Dowling *et al* 2012). Therefore, generation of accurate pseudo-CT images or attenuation maps (μ-maps) from magnetic resonance (MR) images for the purpose of PET attenuation correction (AC) and dose calculation and patient setup in RT planning is highly desired.

Two different approaches have been used for automatic density assignment or the generation of pseudo-CT images in MRI-guided PET AC and RT treatment planning: tissue segmentation and atlas-based methods (Fei *et al* 2012). In the tissue segmentation approach, a μ-map is generated using tissue segmentation followed by the subsequent assignment of predefined density (Martinez-Moller *et al* 2009, Bezrukov *et al* 2013). To include bony structures, a specialized dual ultra-short echo time (dUTE) sequence, able to capture transient signals from components with a short T_2 relaxation time and consequently distinguish bone from air (Keereman *et al* 2010, Berker *et al* 2012, Edmund *et al* 2014), was used. However, this sequence suffers from a long acquisition time, low signal-to-noise ratio, partial volume artefacts and bone prediction errors (Rank *et al* 2013). On the other hand, atlas-based pseudo-CT generation can be implemented using conventional MR sequences where bone/air ambiguity in the MR images is compensated through the utilization of prior knowledge existing in one or multiple atlases of paired CT/MR images aligned to the target MRI spatial coordinates (Dowling *et al* 2012, Arabi and Zaidi 2014, Burgos *et al* 2014, Uh *et al* 2014). In combination with atlas registration, machine learning techniques have been exploited to generate patient-specific μ-map (Hofmann *et al* 2008, Hofmann *et al* 2011, Chen *et al* 2014). In addition to the above-described pseudo-CT generation methods, joint reconstruction of the activity and attenuation-exploiting time-of-flight capability of PET was proposed as an alternative (Rezaei *et al* 2012). In this method, the activity distribution and μ-map are estimated iteratively in an alternate way where the prior knowledge present in MRI can be incorporated to constrain the final solution space (Mehranian and Zaidi 2015).

It has been demonstrated that atlas-based methods are potentially able to generate reliable pseudo-CT images from conventional MR sequences outperforming conventional segmentation-based approaches that neglect bone, thus leading to more accurate PET quantitative accuracy (Hofmann *et al* 2011, Marshall *et al* 2013, Burgos *et al* 2014, Arabi and Zaidi 2016) and RT planning outcomes (Dowling *et al* 2012, Noorda *et al* 2014, Andreasen *et al* 2015, Jonsson *et al* 2015). Several atlas-based methods have been proposed in brain imaging to take the skull into account. Burgos *et al* (2014) developed an approach to generate synthetic CT images using a multi-atlas information propagation scheme where the MRI-derived patient's morphology is locally matched to the aligned dataset of MRI-CT pairs using a robust voxel-wise image similarity measure. Izquierdo-Garcia *et al* presented an approach utilizing statistical parametric mapping (SPM8) software taking advantage of both segmentation and atlas-derived features to generate a robust μ-map for AC of brain PET data (Izquierdo-Garcia *et al* 2014). Similarly in the context of MRI-guided RT planning, Sjölund *et al* (2015) proposed an approach based on a deformable image registration algorithm to generate the electron density of the head from MR images using a novel atlas fusion scheme. An alternative technique enabling the generation of an electron density image without atlas registration is the patch-based pseudo-CT generation approach for RT planning based on a library of MR-CT image patch pairs (Andreasen *et al* 2015). Kapanen *et al* established a relationship between *T*1/*T*2-weighted MRI intensity and CT values for pelvic bone, thus allowing the estimation of patient-specific bone electron density from MRI (Kapanen and Tenhunen 2013).

In this work, we propose a two-step scheme based on the principle of multi-atlas propagation to synthesize a pseudo-CT image from MRI. In the first step, bone segmentation is

optimized on the target MRI. The obtained bone label is then utilized together with the morphological similarity between target and atlas images to define voxel-wise weights for the atlas fusion task. The proposed method is developed to excel in bone identification for the purpose of μ-map generation and MR-only and/or PET/MRI-guided RT treatment planning (Paulus *et al* 2016). This method is evaluated through comparison with conventional segmentation and atlas-based methods using as metrics the accuracy of bone extraction, quantitative analysis of tracer uptake and dose distribution errors in the pelvic region.

2. Materials and methods

2.1. Image acquisition and processing

The patient population consisted of 12 patients presenting with rectal cancer (loco-regionally advanced rectal disease, where the disease spreads only within the region in which it arose as opposed to the metastatic disease) who underwent whole body ^{18}F-FDG PET/CT and PET/MRI examinations. The study protocol was approved by the institutional ethics committee and all patients gave informed consent. A single injection of ^{18}F-FDG (171 $\pm$ 30 MBq) was used to perform both studies sequentially. The PET/CT scans were performed on a Biograph 64 TruePoint scanner (Siemens Healthcare, Erlangen, Germany). After a localization scout scan, an unenhanced low-dose CT scan (120 kVp, 60 mAs, 24 $\times$ 1.5 collimation, a pitch of 1.2, and 1 s per rotation) was performed for AC. PET data acquisition started 146.2 $\pm$ 20 min post-injection with a 3 min per bed position for a total of five to six beds, resulting in a total acquisition time of 15–18 min.

PET/MRI data acquisition was carried out on the Ingenuity TF PET/MRI scanner (Philips Healthcare, Cleveland, OH, USA) (Zaidi *et al* 2011). The proposed MRI-derived pseudo-CT generation approach uses an MRI Dixon volumetric interpolated T1-weighted sequence (Dixon 1984) for pelvis examination with the following parameters: flip angle 10°, TE_1 1.1 ms, TE_2 2.0 ms, TR 3.2 ms, 360 $\times$ 360 mm^2 transverse field-of-view 0.75 $\times$ 0.75 $\times$ 0.75 mm^3 voxel size, and a total acquisition time of 4.5 min.

Due to the temporal difference between PET/CT and MR examinations, a combination of rigid and non-rigid registrations based on normalized mutual information was employed to ensure appropriate inter-modal spatial image matching as described in previous work (Akbarzadeh *et al* 2013). The PET/CT data were employed whereas only the in-phase MR images from the PET/MRI scan were used in this work. The accuracy of the alignment between co-registered MR and CT images was carefully checked visually.

MR images usually suffer from the presence of statistical noise and corruption due to the low-frequency bias field (intra-patient intensity non-uniformity) as well as inter-patient intensity inhomogeneity (Lotjonen *et al* 2010). To minimize the adverse effect of the aforementioned factors, in-phase images of all patients underwent the following pre-processing corrections. Gradient anisotropic diffusion filtering was employed using a conductance of 4, 10 iterations and a time-step of 0.01 to suppress statistical noise while preserving prominent features and signals in the MR images. Afterwards, N4 bias field correction (Tustison *et al* 2010) was employed to remove low-frequency intensity non-uniformity present within subjects (considered as a potential confounder in various image analysis tasks) using a B-spline grid resolution of 400, a number of iterations equalling 200, a convergence threshold of 0.001, a B-spline order of 3, a spline distance of 400, a histogram bins number of 256, and a shrink factor of 3. Histogram matching (McAuliffe *et al* 2001) with a histogram level of 512 and match points equalling 64 was utilized to address inter-subject intensity inhomogeneity in MR images.

2.2. Pseudo-CT image generation

The atlas database is built based on pairs of spatially-aligned (MRI to CT) in-phase Dixon MRI and CT pelvic images. In the first step, all atlas MR images are registered to the target MR image through a leave-one-out cross-validation (LOOCV) scheme. Inter-subject coordinate mapping was obtained using a combination of rigid and non-rigid registration based on normalized mutual information and B-spline interpolator as described previously (Akbarzadeh *et al* 2013). The registrations were performed using Elastix open source software (Klein *et al* 2010). Given the transformation maps, all CT images in the atlas database are then mapped to the target MR image using the corresponding transformation maps.

Given these series of MR/CT pairs, a two-step atlas fusion framework was proposed to create MRI-guided pseudo-CT. In the first step, bone segmentation of the target MRI is optimized through a voxel-by-voxel atlas voting scheme. The output of the first step is a binary bone map of the target subject, which can be assumed to represent the most likely bone delineation of the target image. The rationale behind this step is that bone identification is the major challenge and most important part of MRI-based μ-map generation. This enables us to achieve atlas fusion with special emphasis on bony structures. Given an initial estimation of the target bone, prior knowledge from atlas CT images can be utilized to establish a similarity assessment between them and the estimated target bone to define the weights accordingly for the atlas fusion task. In the second step, to generate a continuous-valued μ-map, an atlas fusion framework is locally optimized according to the resemblance to the obtained target bone map and the morphological similarity to the target MR image. To formulate this process, we use M_n to denote aligned training MRIs, which are continuous-valued intensity images with the corresponding bone label maps L_n. The binary bone label maps are obtained by applying an intensity threshold on the corresponding aligned CT images (atlas CT images after registration) using a Hounsfield unit (HU) value of 140. The primary goal of the first step is to estimate the most likely bone label map ($\widehat{L}$) associated with the target MR image (T). We employed a joint probability of the label map and image intensity given the training data.

$$\widehat{L} = \arg\max_L p(L, T|\{M_n, L_n\}). \tag{1}$$

Here, n denotes the index of training subjects in the atlas dataset. We devised our model based on the assumption that the target MR image (T) can be a product or mixture distribution of either one or some of the training MR images (M_n) whose indices are unknown. In particular, the contribution of the training images is allowed to vary spatially (voxel-by-voxel). To formulate this relationship, a latent random variable ($C(x)$) is defined to specify the indices of the contributory training images at each voxel (x) in the target image (T). To simplify the optimization problem, we assume that the MR intensity values $T(x)$ and the corresponding bone label $L(x)$ are conditionally independent (Zhuang and Shen 2016). However, given the latent random variable ($C(x)$), a relationship is established between them in such a way that in this model $T(x)$ and $L(x)$ are bound together via ($C(x)$). At a later stage, we will determine the relationships between training MR images (M_n) and the target MRI (T) as well as the target bone label (L) and training atlas bone label (L_n). Therefore, the initial conditional independence assumption, which might seem simplistic at first glance, is compensated by $C(x)$ which establishes implicit dependency between the bone label and MR intensity. Given the condition that each voxel in the target MR image is derived from a single training image specified by $C(x)$, the generative model of the target MR image and its corresponding label map through the conditional probability would be

$$p((L,T|C,\{M_n,\ L_n\})) = \prod_x (p(L(x),T(x)|C(x),\{M_n,\ L_n\})).$$

As mentioned earlier, $L(x)$ and $T(x)$ are assumed to be conditionally independent. Therefore, the above conditional probability can be split into two multiplicative terms (Zhuang and Shen 2016):

$$(p(L(x),T(x)|C(x),\{M_n,\ L_n\})) = (p(L(x)|C(x),\{L_n\}) \times p(T(x)|C(x),\{M_n\})).$$

To simplify the problem, marginalization was calculated over the introduced latent variable $C(x)$, resulting in the following formulation:

$$p((L,T|\{M_n,\ L_n\})) = \sum_C p(C) \prod_x (p(L(x),T(x)|C(x),\{M_n,\ L_n\})).$$

Since there is no prior assumption about the degree of contribution of the atlas images to the final bone label map, $C(x)$ takes a constant value ($P(C(x)) = \text{Const.}$). Therefore, the bone segmentation would turn into the form:

$$\widehat{L}(x) = \arg\max_L \sum_{n=1}^{N} p_n((T(x)|M_n(x)))\ p_n((L(x)|L_n(x))). \tag{2}$$

where N is the number of training subjects in the atlas dataset. Considering equation (2), the estimated bone label at each voxel ($\widehat{L}(x)$) depends on the image morphology likelihood $p_n(T(x),M_n(x))$ between the target and the atlas MR images together with the second term $p_n(L(x),L_n(x))$ which is called label prior ($L(x)$ is the bone label of the target image). The main objective in defining the image morphology likelihood is to give greater weights to similar atlases. To achieve this goal, the similarity measure has to provide discriminative information about the underlying structures and at the same time be robust to intensity variation across patients. The phase congruency map (PCM) has been shown to be a robust image feature against the inter-subject intensity variation and provides valuable information about the prominent structures of the image (Kovesi 2000). In the PCM, the local Fourier components of the image are all in phase (congruent) in locations where there are meaningful edges in the image. A PCM can be used to detect structural characteristics of an image, such that it is invariant to image intensity and adequately robust to noise (Kovesi 2000). Equation (3) calculates the phase congruency of an image at location x where $\text{En}_{\text{loc}}(x)$ represents the local energy of the image defined as $\text{En}_{\text{loc}}(x) = \sqrt{F^2(x) + H^2}$, where $F(x)$ is the image signal with its DC component removed, H is the Hilbert transform of $F(x)$, and T_{r} is an offset to avert the effect of noise on the calculation of the local energy ($T_{\text{r}} = M_{\text{r}} + k\sigma_{\text{r}}$). The mean noise response (M_{r}) and variance σ_{r}^2 represent the Rayleigh distribution of the noise energy response. k usually takes a value of 2 or 3; F_m indicates the amplitude of the mth Fourier component, and ε is a small value to avoid division by 0 (Kovesi 2000, Ortiz and Martel 2012). Figure 1 depicts a representative example of PCM computation on the target and one of the MR images from the atlas dataset. The prominent signal in the original images is nicely reflected on PCMs regardless of intensity variation and noise.

$$\text{PCM}(x) = \frac{\lfloor \text{En}_{\text{loc}}(x) - T_{\text{r}} \rfloor}{\sum_m F_m(x) + \varepsilon}. \tag{3}$$

Considering the PCM as a proper image feature measure, we adopted a Gaussian distribution on the PCM of target and MR atlas images with a stationary variance σ^2 as the

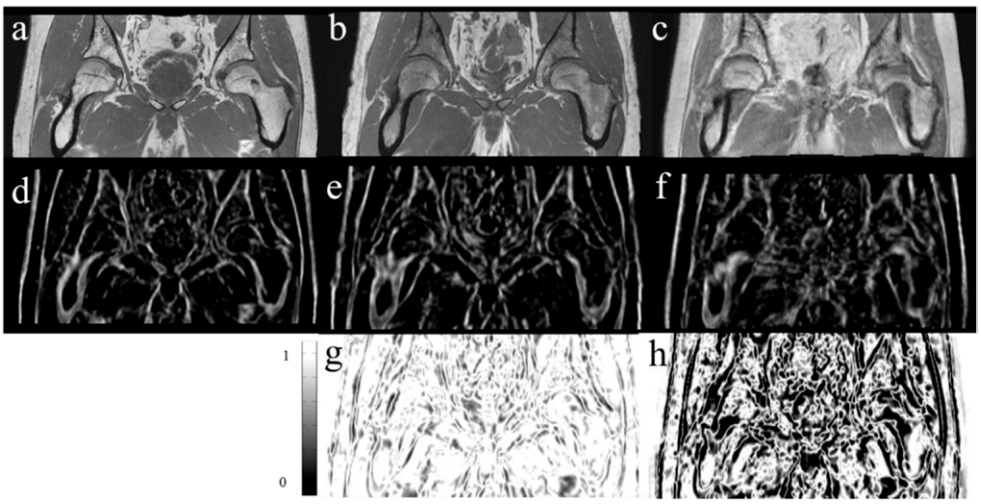

Figure 1. Representative slice of MR images and their corresponding PCMs. (a) Target MR image; (b) well-aligned atlas MR image; (c) poorly-aligned atlas MR image; (d) PCM of image (a); (e) PCM of image (b); (f) PCM of image (c); (g) morphology likelihood between (a) and (b) using equation (4); and (h) morphology likelihood between (a) and (c) using equation (4).

image morphology likelihood term (equation (4)). A representative example of equation (4) is depicted in figure 1.

$$p_n((T(x)|M_n(x))) = \frac{1}{\sqrt{2\pi\sigma^2}} \exp\left[-\frac{1}{2\sigma^2}(\mathrm{PCM}(T(x)) - \mathrm{PCM}(M_n(x)))^2\right]. \tag{4}$$

On the other hand, to define the label prior term $p_n((L(x)|L_n(x)))$, a signed distance transform from the bone label map (L_n) of the atlas dataset was computed; based on which a label prior term was formed via

$$p_n((L(x)|L_n(x))) = \frac{1}{\mathrm{Nr}(x)} \exp(\rho D_n(x)) \tag{5}$$

where $D_n(x)$ denotes the signed distance transform of the bone label map on the training subject n, which is assumed to be positive inside bony structures and negative otherwise; $\rho > 0$ is the slope constant, and $\mathrm{Nr}(x) = \sum_{t=1}^{2} \exp(\rho D_n^t(x))$ is the partition function used for normalization, where the summation is over the number of labels (here equal to 2—background and bone). A representative image of a binary bone mask and its corresponding bone probability map calculated using equation (5) is given in figure 2.

The output of this step ($\widehat{L}$) is presumed to be the most likely bone segmentation of the target MR image. In the next step, this bone segmentation, which is a binary map, is used as a baseline to evaluate the registration accuracy and define weighting factors for each subject of the training dataset. To generate continuously valued pseudo-CT images, the atlas fusion task is achieved through equation (6) where $\mathrm{ACT}_n(x)$ is the CT value of the nth atlas image at voxel x.

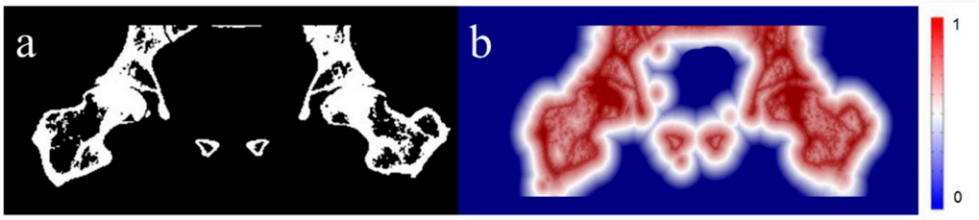

Figure 2. (a) Representative slice of a binary bone mask obtained by intensity thresholding at 140 HU and (b) its corresponding bone probability map calculated using equation (5).

$$\mathrm{LW}(x) = \frac{\sum_{n=1}^{N} \omega_n(x) \times \mathrm{ACT}_n(x)}{\sum_{n=1}^{N} \omega_n(x)} \tag{6}$$

where $\omega_n(x)$ indicates the weighting factor determining the contribution of the nth atlas at voxel x to generate the final locally-weighted pseudo-CT (LW). It is defined as:

$$\omega_n(x) = \frac{1}{\sqrt{2\pi\alpha^2}} \exp\left[-\frac{1}{2\alpha^2}(\mathrm{PCM}(T(x)) - \mathrm{PCM}(M_n(x)))^2\right] \times \frac{1}{\sqrt{2\pi\delta^2}} \exp\left[-\frac{1}{2\delta^2}(D_n(x) - D_{\mathrm{B}}(x))^2\right] \tag{7}$$

where D_{B} indicates the signed distance transform of the obtained bone label of the target image ($\widehat{L}$). The first term in equation (7) measures the morphological similarity between the target and nth atlas MR image (as described in equation (4)) while the second term estimates the resemblance of the nth CT atlas image with respect to the presumably ground truth bone segmentation of the target MR image ($\widehat{L}$). The two Gaussian distributions are adjusted using stationary variances α^2 and δ^2. The free parameters in the above equations, namely α, δ, ρ and σ, were optimized via LOOCV and a parameter-sweeping scheme. To find the optimum value for each parameter, a range of reasonable values was assigned to the chosen parameter while the remaining parameters were kept fixed. Then, the value maximizing the accuracy of extracted bone in the final pseudo-CT image is selected. The free parameters α, δ, ρ and σ took values of 0.3, 0.25, 1.2, and 0.23, respectively.

2.3. Comparison of pseudo-CT images

The pseudo-CT images produced by the proposed method, referred to as local weighting (LW), was compared with reference CT images (in their original spatial coordinates) as well as two other commonly-used methods to generate pseudo-CT images. A common approach adopted for AC on hybrid PET/MRI scanners is MR image segmentation of the body into a number of tissue classes followed by the assignment of predefined LACs to each tissue class. The Philips Ingenuity TF PET/MR uses a three-class μ-map consisting of air, lung and soft-tissue to which the following attenuation coefficients are assigned: $0\,\mathrm{cm}^{-1}$ ($-1\,000$ HU), $0.022\,\mathrm{cm}^{-1}$ (-770 HU), and $0.096\,\mathrm{cm}^{-1}$ (0 HU), respectively (Hu *et al* 2009). In-phase MR images underwent body contour segmentation through connected-component analysis of the low intensity surrounding air voxels initiated by manual seeds using ITK-SNAP image processing software (Yushkevich *et al* 2006). A LAC of $0\,\mathrm{cm}^{-1}$ ($-1\,000$ HU) was assigned

to the surrounding air and $0.096\,\mathrm{cm}^{-1}$ (0 HU) to the body volume (figure 3(c)) to produce a *water-only* μ-map.

The second μ-map evaluated in this work is also generated using a multi-atlas registration approach. Given a series of aligned CT images to the target MR image, the pseudo-CT image is generated by assigning the median value (MV) of the CT numbers across the entire atlas images for each voxel independently (equation (8)).

$$\mathrm{MV}(x) = \mathrm{median}(\mathrm{ACT}_1(x), \ldots, \mathrm{ACT}_n(x)) \tag{8}$$

This approach is equivalent to the well-known majority voting method described in Sjölund *et al* (2015). The major advantage of the median compared to the mean is its robustness to outliers and ability to better deal with multimodal distributions. Figure 3(d) shows a representative example of the MV μ-map.

2.4. Image reconstruction and data analysis

The proposed pseudo-CT generation technique was evaluated using three different metrics, including accuracy of bone extraction, PET quantification bias and error in calculated dose distributions in RT treatment planning. A comparison with the aforementioned techniques was also performed using CT images as references.

2.4.1. Bone extraction. The evaluation of bone volume extraction (three-dimensional (3D)) using the various pseudo-CT images was carried out by comparing the segmented bone from the reference CT images using two volume-based measures, including the Dice similarity coefficient (DSC) (Dice 1945) and relative volume difference (RVD) (Uh *et al* 2014).

$$\mathrm{DSC}(A,Z) = \frac{2|A \cap Z|}{|A| + |Z|}, \quad \mathrm{RVD}(A,Z) = 100 \times \frac{|A| - |Z|}{|A|}$$

where, A is the segmented bone from the reference CT image and Z denotes the extracted bone obtained the pseudo-CT images. Paired t-test analysis was used to assess if the differences between the obtained results are statistically significant using a threshold of 0.05.

2.4.2. Quantitative PET analysis. The generated pseudo-CT images of 12 patients were used for AC of the corresponding PET data. PET images were reconstructed by means of the e7-tool (Siemens Healthcare, Knoxville, TN) using an ordinary Poisson ordered subset expectation maximization iterative reconstruction algorithm. Default parameters (four iterations, eight subsets, and a post-processing Gaussian kernel with a FWHM of 5 mm) adopted in clinical protocols were applied. PET image reconstruction was performed four times for each clinical study using μ-maps derived from CT (PET-CTAC) used as a reference, water-only (PET-water), the pseudo-CT generated by the MV (PET-MV) and LW approaches (PET-LW). The differences between the AC techniques were quantified in terms of the change in the standard uptake value (SUV). Voxel-based relative mean bias (RMB) and relative mean absolute bias (RMAB) were computed for bone, fat and soft-tissue classes using equations (9) and (10), respectively.

$$\mathrm{RMB} = 100 \times \frac{\sum_v (P_v - \mathrm{PCT}_v)}{\sum_v \mathrm{PCT}_v} \tag{9}$$

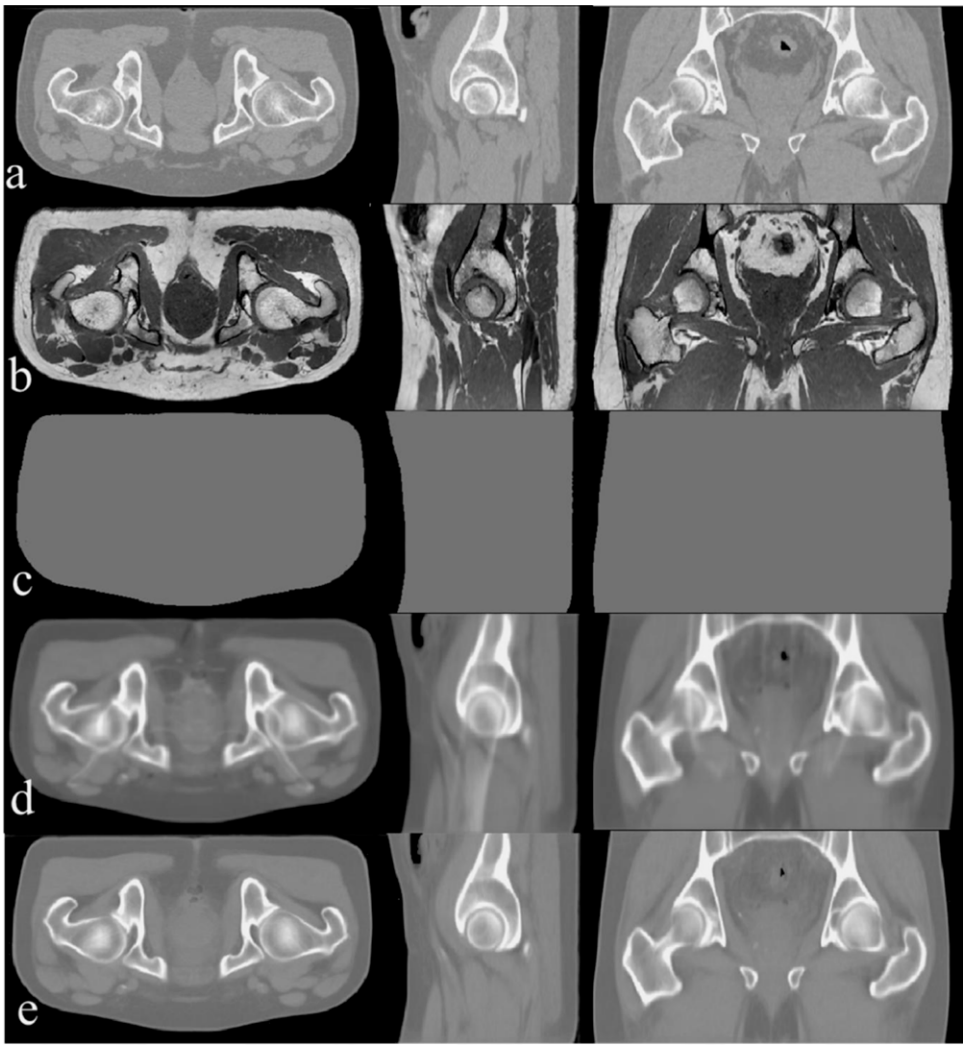

Figure 3. (a) Reference CT; (b) target MRI; (c) water-only μ-map; (d) pseudo-CT generated using the MV technique; (e) pseudo-CT generated using the LW atlas fusion method.

$$\mathrm{RMAB} = 100 \times \frac{\sum_v |P_v - \mathrm{PCT}_v|}{\sum_v \mathrm{PCT}_v} \tag{10}$$

where P_v denotes the SUV value of voxel v in PET images corrected for attenuation using the pseudo-CT images, and PCT stands for the corresponding reference PET-CTAC. The segmentation of tissue classes was performed based on CT HUs using the following thresholds: bone if the HU $\geqslant 140$, soft-tissue if $-20 < \mathrm{HU} \leqslant 140$, and fat if $-350 < \mathrm{HU} \leqslant -20$.

2.4.3. Dose distribution analysis The volumetric-modulated arc therapy (VMAT) technique was employed for treatment planning using the Eclipse™ treatment planning system (Varian

Medical Systems Inc., Palo Alto, CA). RT treatments were performed by irradiating target volumes defined on the rectum and prostate. The dose differences were calculated on target volumes consisting of the gross target volume (GTV), the clinical target volume (CTV), the planning target volume (PTV), the rectum and prostate. The patients received radiation doses varying between 45 and 60 Gy with a mean dose of 1.5–2 Gy in 30 fractions targeting the PTV. In addition to target volumes, the dose calculation was also performed for in-field OAR including the left and right femur, bladder, bowel bag, anus, spinal cord, iliac crest, genitalia, vagina (two patients), uterus (two patients), penile bulb and bladder wall for each patient. The same structure set was associated with both the reference CT and pseudo-CTs as they were generated in the same spatial coordinates. All volume and organ delineations were performed by a radiation oncologist on the target MRI and were then copied on the reference CT and pseudo-CT images. The dose calculation was carried out on each patient's pseudo-CT. The treatment plans were then transferred to the reference CT images and recalculated using same structure set and monitor units. The field-of-view and number of slices were kept identical on each image series ensuring matched organ contours. Dose volume histograms (DVHs) and dose distribution maps were exported for both the reference CT and pseudo-CTs. The DVH represents a histogram relating the radiation dose to the tissue volume in RT planning, summarizing 3D dose distributions in a 2D graphical format. The 'volume' term in DVH analysis stands for a target of radiation treatment or a healthy OAR. Dose calculations were performed using the anisotropic analytical algorithm (AAA v. 10) for a 6 MV photon beam and a dose matrix of $2.5 \times 2.5 \times 2.5\,\mathrm{mm}^3$.

For dose comparisons, the absorbed 'Dose-max', 'Dose-min' and 'Dose-mean' to the target volumes and the OAR were compared (equation (11)) between plans optimized on the reference CT and pseudo-CT images, considering $\mathrm{Dose}_{\mathrm{CT}}$ and $\mathrm{Dose}_{\mathrm{pCT}}$ as the measured dose in the plan calculated on CT and pseudo-CT images, respectively.

$$\mathrm{Difference} = 100 \times \frac{\mathrm{Dose}_{\mathrm{pCT}} - \mathrm{Dose}_{\mathrm{CT}}}{\mathrm{Dose}_{\mathrm{CT}}}. \tag{11}$$

Moreover, the DVHs of different organs were used to evaluate the dosimetric differences between dose distributions calculated using CT and pseudo-CT images. Given the DVH curves, each point on the curves representing a specific dose level was compared with the reference CT. The percentage point deviation was calculated and averaged for all points of DVHs corresponding to each organ absorbed dose using equations (12) and (13) for mean absolute errors (MAEs) and mean errors (MEs), respectively.

$$\mathrm{MAE} = 100 \times \frac{1}{P} \sum_{i=1}^{P} \frac{\left| D_{\mathrm{pCT}}(i) - D_{\mathrm{CT}}(i) \right|}{D_{\mathrm{CT}}(i)} \tag{12}$$

$$\mathrm{ME} = 100 \times \frac{1}{P} \sum_{i=1}^{P} \frac{D_{\mathrm{pCT}}(i) - D_{\mathrm{CT}}(i)}{D_{\mathrm{CT}}(i)} \tag{13}$$

where, P represents the total number of DVH points between 'Dose100%' and 'Dose 0%' in dose increments of 0.1 Gy, whereas $D_{\mathrm{pCT}}(i)$ and $D_{\mathrm{CT}}(i)$ are the accumulated doses in Gy given to the volume i in the reference CT and pseudo-CT images, respectively.

The calculated dose distributions using the different pseudo-CTs images were compared with the corresponding reference CTs and the volume (cc) receiving a certain amount of different dosage was measured. To this end, the dose difference maps were computed through the voxel-by-voxel subtraction of dose values calculated on pseudo-CTs from those of the reference CT. Then, at each dose difference level, the associated volume was computed.

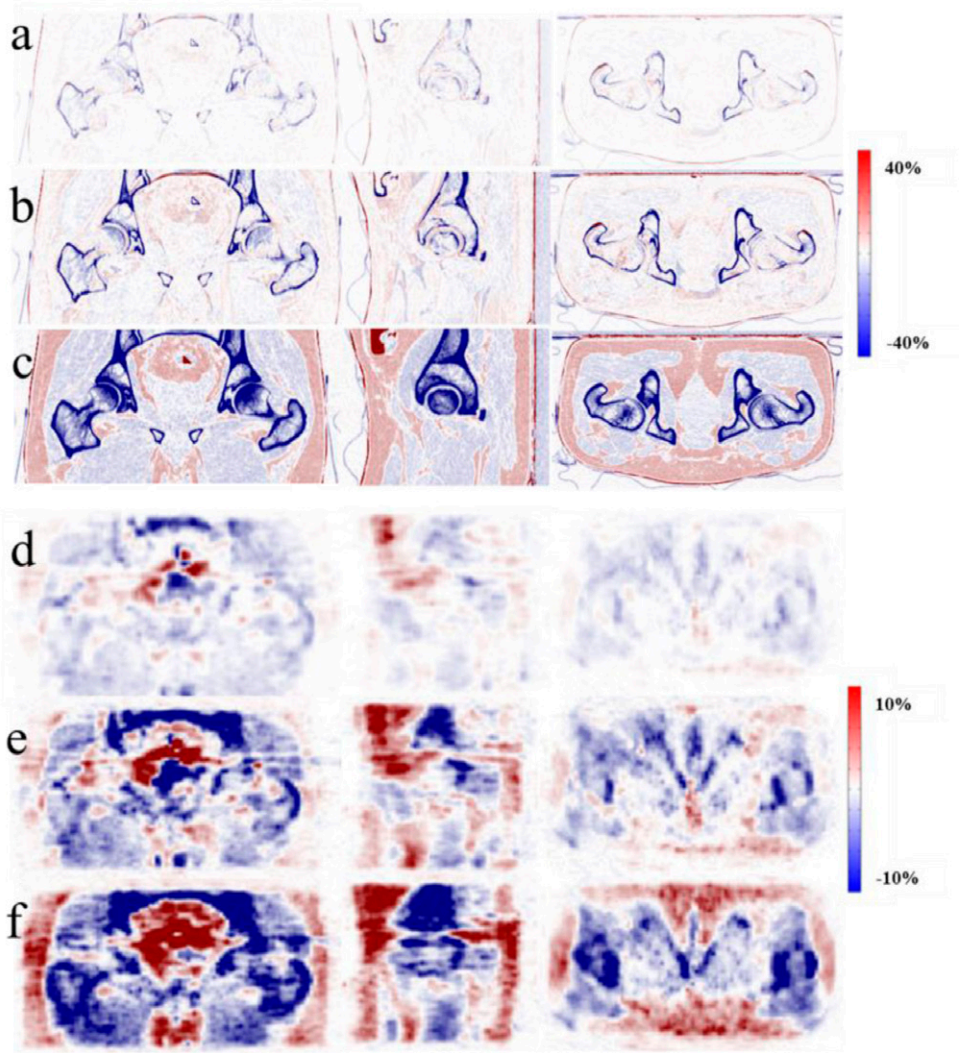

Figure 4. Representative slices of attenuation error maps for (a) LW; (b) MV; (c) water-only and SUV bias maps for (d) LW; (e) MV; (f) water-only methods.

The measured volumes were plotted versus dose discrepancy ranging from −1 to 1 Gy. Moreover, 2D gamma analysis (Jonsson *et al* 2013) (evaluated at 2%/2 mm and 1%/1 mm dose difference/distance to agreement) was used to analyze axial dose distributions intersecting the isocenter. The Gamma test is a widely-used metric for comparing dose distributions, which combines features of dose difference and distance-to-agreement (Low *et al* 1998).

Table 1. Accuracy of extracted bone (mean ± SD) from pseudo-CT images derived using LW and MV approaches.

	MV	*P*-value	LW	*P*-value
DSC	0.75 ± 0.10	0.07	0.89 ± 0.06	<0.05
RVD (%)	−18.9 ± 03.8	0.05	−10.9 ± 03.1	0.05

Table 2. Voxel-wise relative mean ± SD (absolute mean ± SD) SUV bias for PET images corrected for attenuation using the different pseudo-CT images.

	Fat	Soft-tissue	Bone
	Mean ± SD	Mean ± SD	Mean ± SD
Method	(absolute mean ± SD)	(absolute mean ± SD)	(absolute mean ± SD)
Water-only	7.5 ± 8.3	−5.4 ± 6.2	−19.9 ± 11.8
	(8.3 ± 6.8)	(9.8 ± 6.8)	(21.1 ± 9.9)
LW	2.2 ± 5.5	−2.0 ± 4.1	−1.5 ± 5.0
	(5.6 ± 4.5)	(5.0 ± 3.9)	(4.1 ± 2.2)
MV	4.9 ± 6.1	−4.0 ± 6.2	−8.1 ± 8.2
	(7.7 ± 5.9)	(7.1 ± 5.2)	(11.1 ± 6.2)

Table 3. Dosimetric errors (relative mean ± SD (absolute mean ± SD)) for OAR calculated using the total number of DVH points between $D_{100\%}$ and $D_{0\%}$ in dose increments of 0.1 Gy employing equations (12) and (13).

	Water-only	MV	LW
Region (OAR)	ME ± SD (MAE ± SD)	ME ± SD (MAE ± SD)	ME ± SD (MAE ± SD)
Femur R	−4.0 ± 3.5 (5.3 ± 1.1)	−2.2 ± 1.6 (3.1 ± 1.0)	−0.3 ± 1.3 (1.2 ± 0.4)
Femur L	−3.9 ± 2.9 (4.8 ± 1.2)	−2.2 ± 1.9 (3.2 ± 0.9)	0.5 ± 1.0 (1.1 ± 0.5)
Bladder	2.5 ± 2.4 (3.2 ± 1.4)	1.4 ± 1.4 (3.3 ± 0.9)	0.4 ± 1.4 (1.0 ± 0.4)
Bowel bag	1.4 ± 1.9 (3.6 ± 1.2)	0.9 ± 1.9 (3.2 ± 1.1)	0.1 ± 1.6 (0.9 ± 0.5)
Anus	3.3 ± 2.5 (4.6 ± 1.5)	−0.6 ± 2.3 (3.1 ± 0.9)	−0.3 ± 1.2 (1.0 ± 0.4)
Spinal cord	3.7 ± 2.6 (4.4 ± 1.6)	1.5 ± 2.0 (3.3 ± 1.0)	0.8 ± 0.9 (1.2 ± 0.4)
Iliac crest	−3.2 ± 2.8 (4.3 ± 1.2)	2.1 ± 1.7 (3.0 ± 0.8)	−0.4 ± 1.1 (1.2 ± 0.5)
Genitalia	3.5 ± 2.7 (4.2 ± 1.1)	−2.8 ± 1.9 (3.1 ± 0.9)	0.7 ± 1.6 (1.1 ± 0.6)
Penile bulb	1.1 ± 2.5 (4.1 ± 1.2)	−1.4 ± 1.3 (2.8 ± 0.6)	−0.5 ± 1.1 (1.0 ± 0.4)
Bladder wall	3.7 ± 2.7 (4.2 ± 1.5)	0.6 ± 1.5 (2.6 ± 0.7)	0.5 ± 1.0 (1.2 ± 0.3)
Uterus (2 patients)	1.6 ± 2.8 (4.6 ± 1.6)	1.8 ± 1.9 (3.0 ± 0.8)	0.6 ± 0.9 (1.8 ± 0.5)
Vagina (2 patients)	3.5 ± 2.9 (4.8 ± 1.4)	2.7 ± 2.9 (4.4 ± 1.1)	0.8 ± 0.8 (1.3 ± 0.6)

Table 4. Dosimetric errors (relative mean ± SD (absolute mean ± SD)) for target regions calculated using the total number of DVH points between $D_{100\%}$ and $D_{0\%}$ in dose increments of 0.1 Gy employing equations (12) and (13).

	Water-only	MV	LW
Region (target)	ME ± SD (MAE ± SD)	ME ± SD (MAE ± SD)	ME ± SD (MAE ± SD)
Prostate	2.1 ± 1.9 (3.2 ± 1.1)	1.2 ± 1.9 (2.8 ± 0.9)	0.4 ± 1.2 (1.2 ± 0.5)
Rectum	2.8 ± 2.6 (3.3 ± 1.2)	−1.3 ± 1.6 (2.9 ± 0.8)	0.3 ± 1.0 (1.0 ± 0.4)
PTV-45	2.4 ± 2.8 (3.0 ± 1.1)	1.3 ± 1.1 (2.5 ± 0.7)	0.4 ± 1.1 (0.9 ± 0.3)
PTV-50	3.5 ± 2.7 (4.0 ± 1.0)	2.6 ± 2.1 (3.2 ± 0.7)	0.1 ± 1.2 (0.8 ± 0.4)
CTV-45	3.2 ± 2.9 (4.2 ± 1.0)	2.0 ± 1.2 (2.9 ± 0.6)	−0.1 ± 1.3 (1.0 ± 0.3)
CTV-50	3.7 ± 2.8 (4.3 ± 0.9)	2.1 ± 2.3 (3.0 ± 0.8)	−0.6 ± 1.4 (1.1 ± 0.5)
GTV	1.3 ± 2.7 (4.0 ± 1.0)	1.0 ± 1.4 (2.9 ± 0.6)	−0.7 ± 1.2 (1.2 ± 0.4)

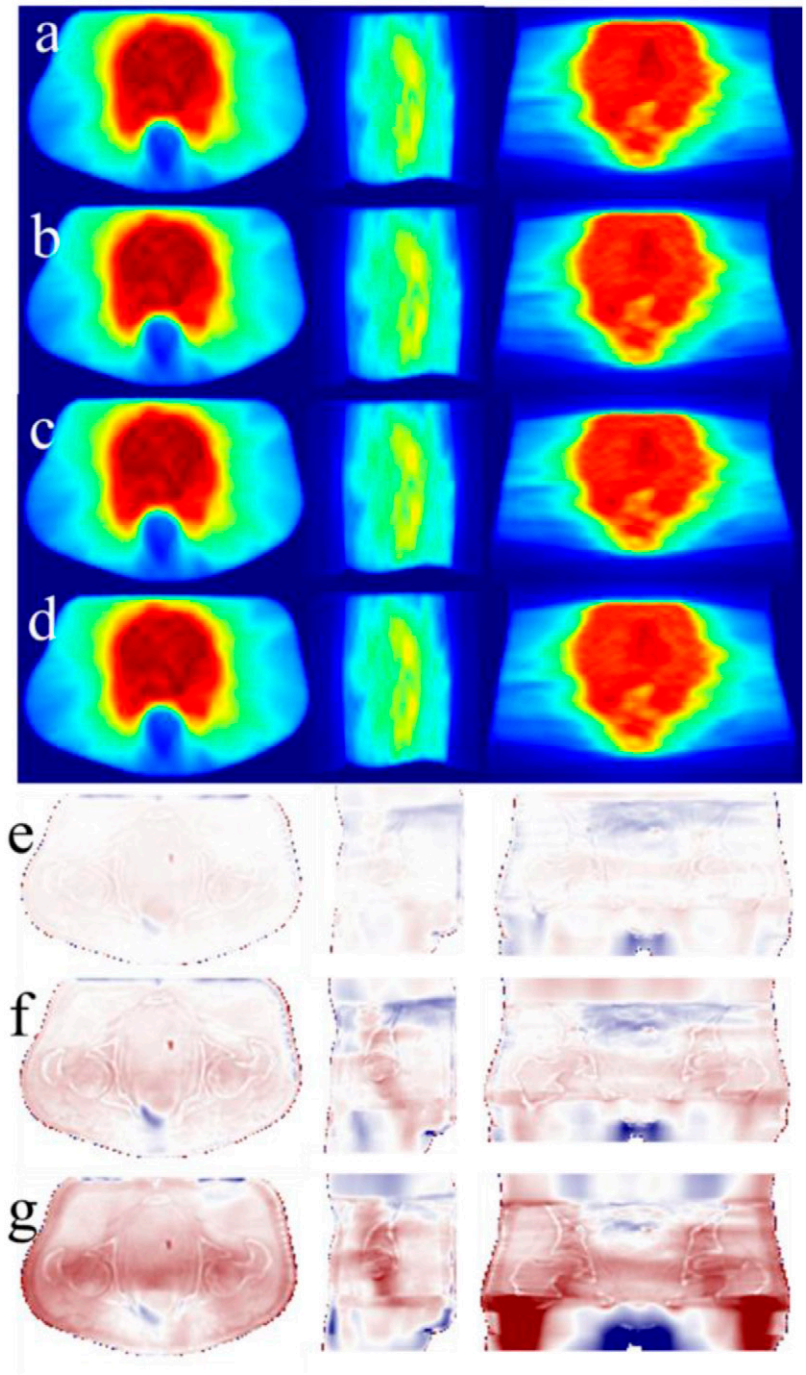

Figure 5. Representative slices of dose distributions calculated using (a) CT, (b) LW pseudo-CT, (c) MV pseudo-CT and (d) water-only. Dose distribution error maps are also shown: (e) LW, (f) MV and (g) water-only.

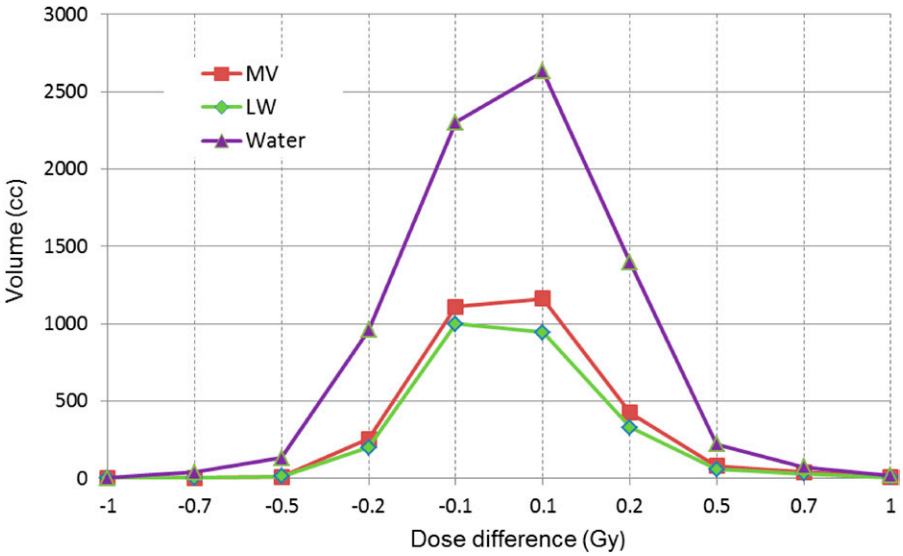

Figure 6. Volumes (cc) associated with a certain magnitude of dose difference (Gy) between dose distributions calculated using reference CT and different pseudo-CT images.

3. Results

Representative slices of the generated pseudo-CTs along with reference MR and CT images are shown in figure 3 where visual inspection reveals the considerable improvement brought by the proposed method in terms of anatomical structures' sharpness. Table 1 summarizes the results of bone extraction accuracy for LW and MV techniques. It can be observed that the LW approach outperforms the other techniques considering all four metrics used (with statistical significance proven only for DSCs and sensitivity). Figure 4 depicts SUV and attenuation bias maps for the different methods for the same slices shown in figure 3. Voxel-wise SUV bias evaluation on PET images corrected for attenuation using different μ-maps considering PET-CTAC as the reference are provided in table 2. Likewise, the LW technique leads to a significant PET quantification bias reduction, particularly in bone tissue.

RT dose distribution calculations performed using the different pseudo-CT images were evaluated based on the resulting DVHs for a number of regions. The results of the analysis are presented separately for target volumes and OAR considering that two out of 12 patients were female. Therefore, ten contours were defined on the prostate and two on the uterus and vagina. Tables 3 and 4 summarize the results of the point-by-point analysis of DVHs between the maximum and minimum absorbed dose in dose increments of 0.1 Gy. Dosimetric errors are reported in terms of relative mean and absolute mean averaged over 12 patients. Figure 5 shows a representative dose distribution map calculated using the various pseudo-CT images along with dose distribution error maps, taking the one calculated using patient-specific CT as a reference. Moreover, the volume associated with a certain magnitude of absolute dose difference is presented in figure 6. The measured volume and absorbed dose differences are averaged over the entire patient datasets.

For each body organ and target volume, the minimum, mean, and maximum absorbed doses calculated using the different pseudo-CT image series were compared. Tables 5 and 6 present the average differences between the dose distributions calculated using the different

Table 5. Average differences (relative mean ± SD) between maximum, mean, and minimum absorbed doses calculated using different pseudo-CT images and reference CT for OAR.

Region (OAR)	Water-only (Diff. dose-max (%) Diff. dose-mean (%) Diff. dose-min (%))	MV (Diff. dose-max (%) Diff. dose-mean (%) Diff. dose-min (%))	LW (Diff. dose-max (%) Diff. dose-mean (%) Diff. dose-min (%))
Femur R	−7.1 ± 4.1	−3.2 ± 1.7	−0.5 ± 1.1
	−3.0 ± 3.2	−2.2 ± 1.5	−0.4 ± 1.0
	−6.2 ± 3.7	−3.0 ± 1.6	−0.5 ± 1.2
Femur L	−5.9 ± 3.9	−2.4 ± 1.7	0.8 ± 1.0
	−4.0 ± 3.2	−2.1 ± 1.4	0.6 ± 0.8
	−4.9 ± 2.7	−2.1 ± 1.5	0.9 ± 1.1
Bladder	3.0 ± 2.5	2.6 ± 1.2	0.7 ± 1.0
	2.8 ± 2.2	2.2 ± 1.3	0.6 ± 0.8
	2.7 ± 2.4	2.3 ± 1.2	0.8 ± 1.1
Bowel bag	2.9 ± 2.0	2.1 ± 2.1	0.9 ± 1.7
	2.8 ± 1.9	2.0 ± 1.8	0.5 ± 1.6
	2.8 ± 2.0	2.3 ± 2.0	0.8 ± 1.5
Anus	3.9 ± 2.5	−1.9 ± 2.3	−0.8 ± 1.4
	3.7 ± 2.6	−1.4 ± 2.0	−0.6 ± 1.3
	3.9 ± 2.6	−1.9 ± 2.1	−0.9 ± 1.5
Spinal cord	4.3 ± 2.6	−2.6 ± 2.1	1.1 ± 1.0
	3.9 ± 2.4	−2.5 ± 1.9	0.8 ± 0.9
	4.0 ± 2.5	−2.4 ± 2.1	1.0 ± 1.0
Iliac crest	−3.9 ± 3.0	−2.6 ± 2.0	−1.0 ± 1.1
	−3.2 ± 2.7	−2.2 ± 1.8	−0.9 ± 1.0
	−4.0 ± 2.9	−2.9 ± 2.2	−1.1 ± 1.1
Genitalia	3.9 ± 2.8	−3.0 ± 2.1	0.9 ± 1.5
	3.6 ± 2.3	−2.8 ± 1.9	0.7 ± 1.4
	4.6 ± 2.8	−2.9 ± 1.9	0.9 ± 1.4
Penile bulb	3.5 ± 2.3	−1.9 ± 1.8	−1.2 ± 1.1
	3.3 ± 2.5	−1.3 ± 1.5	−0.9 ± 1.1
	3.6 ± 2.6	−2.0 ± 1.8	−1.2 ± 1.0
Bladder wall	4.1 ± 2.6	2.7 ± 1.5	0.7 ± 1.1
	3.9 ± 2.5	2.2 ± 1.7	0.5 ± 1.0
	4.5 ± 2.6	2.9 ± 1.6	0.9 ± 1.1
Uterus (2 patients)	3.4 ± 2.7	2.0 ± 1.7	−0.8 ± 1.0
	3.2 ± 2.4	1.5 ± 1.5	−0.6 ± 0.9
	3.5 ± 2.8	2.1 ± 1.9	−0.9 ± 1.1
Vagina (2 patients)	3.6 ± 2.4	2.1 ± 1.9	0.6 ± 1.0
	3.5 ± 2.5	1.6 ± 1.6	0.5 ± 0.9
	3.7 ± 2.7	2.3 ± 2.0	0.7 ± 1.1

pseudo-CT images for both OAR and target volumes, whereas figures 7 and 8 depict representative DVHs of OAR and target volumes. The 2D gamma analysis of isocenter dose distributions evaluated at 2%/2 mm dose difference/distance-to-agreement revealed pass rates

Table 6. Average differences (relative mean ± SD) between maximum, mean, and minimum absorbed doses calculated using different pseudo-CT images and reference CT for target regions.

	Water-only	MV	LW
	(Diff. dose-max (%)	(Diff. dose-max (%)	(Diff. dose-max (%)
	Diff. dose-mean (%)	Diff. dose-mean (%)	Diff. dose-mean (%)
Region (target)	Diff. dose-min (%))	Diff. dose-min (%))	Diff. dose-min (%))
Prostate	2.9 ± 1.6	1.6 ± 2.0	1.1 ± 1.1
	2.2 ± 1.6	1.4 ± 1.9	0.8 ± 10
	2.7 ± 1.5	1.9 ± 2.1	1.1 ± 1.0
Rectum	3.7 ± 2.2	−1.7 ± 1.6	0.6 ± 1.0
	3.1 ± 2.1	−1.2 ± 1.5	0.3 ± 0.9
	3.8 ± 2.4	−1.9 ± 1.6	0.8 ± 1.1
PTV-45	2.8 ± 2.3	1.8 ± 1.0	0.6 ± 1.1
	2.5 ± 2.0	1.6 ± 1.0	0.4 ± 1.0
	3.0 ± 2.1	1.9 ± 1.1	0.5 ± 1.0
PTV-50	4.1 ± 2.1	2.8 ± 2.1	0.6 ± 1.2
	3.9 ± 1.9	2.4 ± 1.7	0.4 ± 1.0
	4.0 ± 2.0	2.6 ± 2.0	1.0 ± 1.1
CTV-45	3.6 ± 2.3	2.6 ± 1.5	−0.7 ± 1.4
	3.2 ± 2.0	2.1 ± 1.2	−0.3 ± 1.0
	3.9 ± 2.4	2.7 ± 1.4	−0.8 ± 1.2
CTV-50	4.2 ± 2.5	3.1 ± 2.6	−1.3 ± 1.2
	4.1 ± 2.2	2.5 ± 2.2	−0.6 ± 1.0
	4.6 ± 2.5	3.2 ± 2.7	−1.5 ± 1.3
GTV	3.8 ± 2.5	1.9 ± 1.4	−1.0 ± 1.2
	3.3 ± 2.4	1.4 ± 1.3	−0.8 ± 1.1
	4.0 ± 2.6	2.0 ± 1.6	−1.1 ± 1.2

of 99.66 ± 0.39%, 99.65 ± 0.70% and 99.86 ± 0.27% (mean ± SD) for water-only, MV and LW, respectively. Reducing the evaluation criteria to 1%/1 mm lowered the pass rates to 91.40 ± 7.56%, 96.00 ± 4.11% and 97.67 ± 3.60, respectively, which remains within clinically-acceptable tolerance.

4. Discussion

We proposed a surrogate CT generation approach using a two-step optimization paradigm to improve the accuracy of bone identification and provide a continuous-valued pseudo-CT image at the same time. In the first step, the segmentation is optimized for bone extraction from the target MRI, whereby prior knowledge from the atlas CT images is utilized to assess the resemblance of bony structures to the target image. Without the initial target bone estimation, the prior knowledge from CT cannot be used in the atlas fusion scheme owing to the lack of supposedly ground truth to compare CT images with. It is worth mentioning that the initial bone estimation does not represent the bone identification in the final pseudo-CT image and only contributes to determine the weights (according to equation (7)) for the atlas fusion scheme. The initial step enhances the accuracy of bone extraction by roughly 10% due

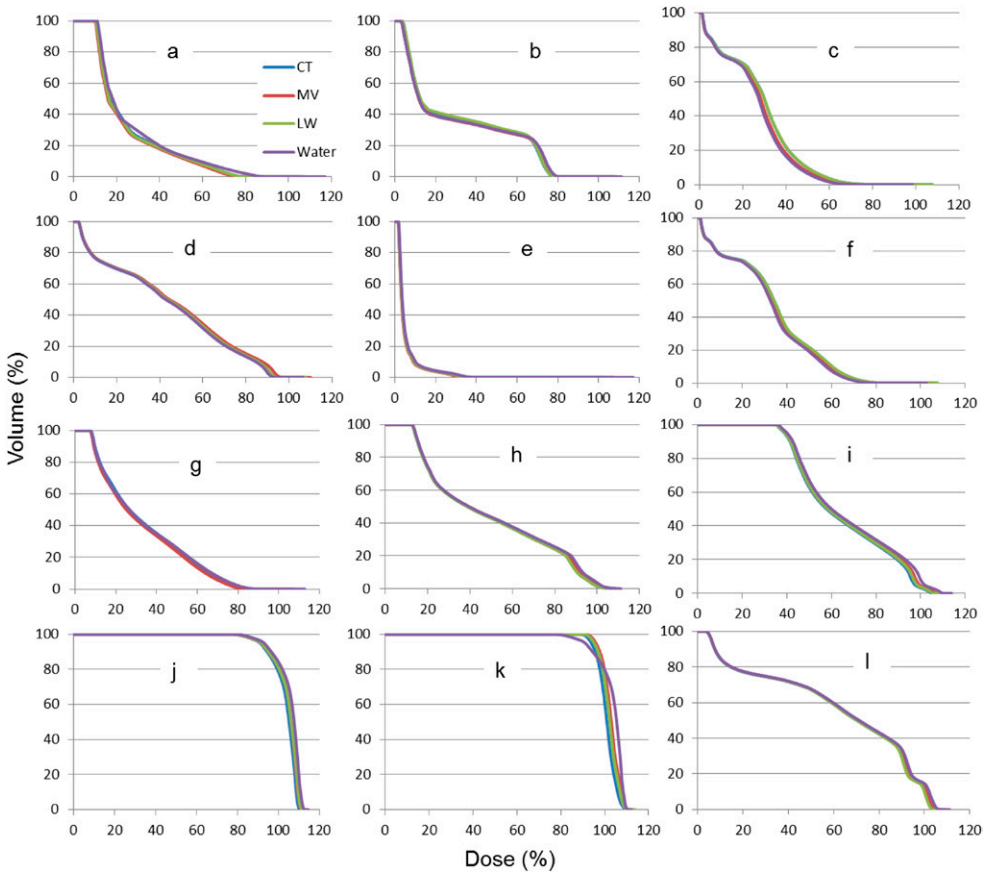

Figure 7. Representative DVHs of dose distributions calculated using different pseudo-CT images for OAR, namely (a) anus, (b) spinal cord, (c) left femur, (d) iliac crest, (e) genitalia, (f) right femur, (g) penile bulb, (h) bladder wall, (i) bladder, (j) uterus, (k) vagina, and (l) bowel bag.

to additional emphasis on bony structures. The improvement observed in bone identification (DSC of 0.89 instead of 0.75) stems from the effective pattern recognition and local misalignment detection provided by the two-step segmentation and fusion optimization scheme. Similar studies were performed using an atlas-based method developed for dose calculation and DRR generation using a conjugate electron density database generated from co-registered CT-MRI scans (Dowling *et al* 2012). Comparisons made using 26 whole-pelvic scans revealed an agreement (based on the DSC metric) of 0.79 ± 0.12 and 0.64 ± 0.16 for the pelvic bone and the bladder, respectively. In a more recent study conducted by Andreasen *et al* (2015), a patch-based pseudo-CT generation method was proposed and compared with a Gaussian mixture regression model using dUTE scans (Johansson *et al* 2011) and a multi-atlas information propagation approach (Burgos *et al* 2014). The patch-based method yielded a DSC of 0.84 for bone volume while the multi-atlas and the Gaussian mixture regression approaches resulted in a DSC of 0.83 and 0.67, respectively. It should be noted that this comparison was performed using cranial MRI/CT scans of five patients.

Voxel-wise evaluation of PET quantification bias indicated the superior performance of the proposed method over water-only (or a three-class MRI segmentation-based μ-map) mostly

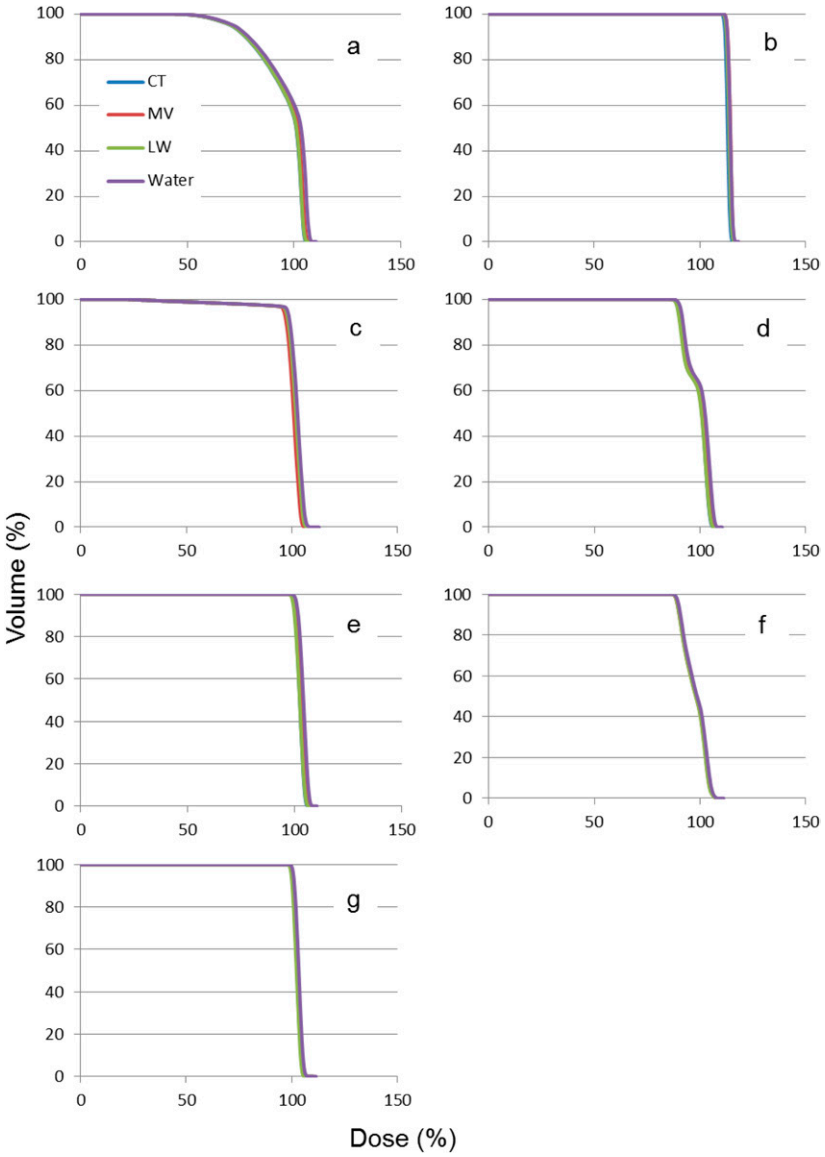

Figure 8. Representative DVHs of dose distributions calculated using different pseudo-CT images for target regions, namely (a) the prostate, (b) GTV, (c) PTV_50, (d) CTV_45, (e) rectum, (f) PTV_45, and (g) CTV_50.

due to the considerable improvement of bone extraction accuracy. Ignoring bony structures (water-only μ-map) resulted in a mean SUV bias of $-19.9 \pm 11.8\%$ while the MV method yielded a mean bias of $-8.1 \pm 8.2\%$. This is in agreement with results reported by Paulus *et al* (2015) where a mean SUV bias of $-25.5 \pm 7.9\%$ was obtained in bone regions using a four-class μ-map ignoring bone, which was reduced to $-4.9 \pm 6.7\%$ using a strategy enabling the incorporation of bony tissue in the μ-map for whole-body PET/MR imaging. Due to the higher photon energy employed in RT (here a 6 MV beam) compared to the energy of annihilation photons (511 keV), dose calculation using a different pseudo-CT image series is less sensitive

to tissue LACs in comparison with PET quantification bias. As such, the dosimetric errors summarized in tables 3 and 4 based on DVH analysis exhibit a smaller range of errors among the different pseudo-CT generation techniques. However, a similar trend to PET SUV bias is observed where a water-only map yielded the largest errors while the LV technique resulted in less than 1% errors for all target volumes and OAR. Similarly, Kapanen and Tenhunen (2013) compared their pseudo-CT generation method against water-only pseudo-CT and reference CT considering a treatment plan for the pelvic region optimized for 15 MeV photons. Maximal dose differences between water-only and their proposed pseudo-CT with respect to reference CT for all points contained within the PTV were 3.7% and 1.2%, respectively. Therefore, our results (tables 3 and 4) are in agreement with the range of dosimetric errors reported in the literature.

Dose comparison results between maximum, mean and minimum absorbed doses in different target volumes and OAR indicated a larger range compared to DVH analysis with a maximum error in large bony structures, such as the left and right femurs. Jonsson *et al* (2015) reported a maximum dose difference of $-5.9 \pm 7.9\%$ using an ultra-short echo time -based pseudo-CT approach in the head region. For the prostate, Kim *et al* (2015) evaluated two pseudo-CT generation methods and reported mean dose errors of 1.22% and 0.54% for both techniques. Apart from the relatively low dosimetric errors achieved using the LW technique, the standard deviation of measured errors, for either the DVH analysis or minimum–maximum dose comparison, exhibited significant reduction compared to those obtained using water-only and MV techniques. Moreover, gamma analysis demonstrated the efficiency of the proposed method where $97.67 \pm 3.60\%$ of voxels passed the evaluation criteria of 1%/1 mm compared to 95.85% reported in another study focusing on the brain region (Jonsson *et al* 2015).

The outcome of this algorithm does not depend on the MRI sequence used as long as the target and training atlas images originate from the same MRI sequence. However, if the used MR sequence provides better image quality in terms of the signal-to-noise ratio, this enhances the performance of the registration algorithm and feature extraction capability, which in turn will improve the outcome.

5. Conclusion

A novel atlas-based pseudo-CT generation approach was proposed using a clinically-available conventional Dixon MRI sequence for the pelvic region. The superior performance of the proposed method was demonstrated using clinical studies in terms of bone identification, reduction in PET quantification bias, and reduction in dose distribution calculation errors for RT treatment planning compared to conventional methods. The proposed method can be easily applied to other body regions, such as the brain, and even to whole-body imaging. The proposed method has promising potential applications in either MRI-only or PET/MRI guided RT treatment planning or MRI-guided AC in hybrid PET/MR imaging.

Acknowledgment

This work was supported by the Swiss National Science Foundation under Grant SNSF 31003 A-149957 and the Swiss Cancer Research Foundation under Grant KFS-3855-02-2016.

References

Ahmed M *et al* 2010 The value of magnetic resonance imaging in target volume delineation of base of tongue tumours—a study using flexible surface coils *Radiother. Oncol.* **94** 161–7

Akbarzadeh A *et al* 2013 Evaluation of whole-body MR to CT deformable image registration *J. Appl. Clin. Med. Phys.* **14** 4163 (PMID: 23835382)

Andersen F L *et al* 2014 Combined PET/MR imaging in neurology: MR-based attenuation correction implies a strong spatial bias when ignoring bone *Neuroimage* **84** 206–16

Andreasen D, Van Leemput K, Hansen R H, Andersen J A and Edmund J M 2015 Patch-based generation of a pseudo CT from conventional MRI sequences for MRI-only radiotherapy of the brain *Med. Phys.* **42** 1596–605

Arabi H and Zaidi H 2014 Comparison of atlas-based bone segmentation methods in whole-body PET/MRI *IEEE Nuclear Science Symp. & Medical Imaging Conf. (Seattle, USA)* pp 1–4

Arabi H and Zaidi H 2016 Magnetic resonance imaging-guided attenuation correction in whole-body PET/MRI using a sorted atlas approach *Med. Image Anal.* **31** 1–15

Berker Y *et al* 2012 MRI-based attenuation correction for hybrid PET/MRI systems: a 4-class tissue segmentation technique using a combined ultrashort-echo-time/dixon MRI sequence *J. Nucl. Med.* **53** 796–804

Bezrukov I, Mantlik F, Schmidt H, Schölkopf B and Pichler B J 2013 MR-based PET attenuation correction for PET/MR imaging *Semin. Nucl. Med.* **43** 45–59

Brunt J N 2010 Computed tomography-magnetic resonance image registration in radiotherapy treatment planning *Clin. Oncol.* **22** 688–97

Burgos N *et al* 2014 Attenuation correction synthesis for hybrid PET-MR scanners: application to brain studies *IEEE Trans. Med. Imaging* **33** 2332–41

Cattaneo G M *et al* 2005 Target delineation in post-operative radiotherapy of brain gliomas: interobserver variability and impact of image registration of MR (pre-operative) images on treatment planning CT scans *Radiother. Oncol.* **75** 217–23

Chen Y *et al* 2014 MRI based attenuation correction for PET/MRI via MRF segmentation and sparse regression estimated CT *11th Int. Symp. on Int. Biomedical Imaging (ISBI)* pp 1364–7

Dice L R 1945 Measures of the amount of ecologic association between species *Ecology* **26** 297–302

Dickson J C, O'Meara C and Barnes A 2014 A comparison of CT-and MR-based attenuation correction in neurological PET *Eur. J. Nucl. Med. Mol. Imaging* **41** 1176–89

Dixon W T 1984 Simple proton spectroscopic imaging *Radiology* **153** 189–94

Dowling J A *et al* 2012 An atlas-based electron density mapping method for magnetic resonance imaging (MRI)-alone treatment planning and adaptive MRI-based prostate radiation therapy *Int. J. Radiat. Oncol. Biol. Phys.* **83** e5–11

Edmund J M *et al* 2014 A voxel-based investigation for MRI-only radiotherapy of the brain using ultra short echo times *Phys. Med. Biol.* **59** 7501

Fei B *et al* 2012 MR/PET quantification tools: registration, segmentation, classification, and MR-based attenuation correction *Med. Phys.* **39** 6443–54

Hofmann M *et al* 2008 MRI-based attenuation correction for PET/MRI: a novel approach combining pattern recognition and Atlas registration *J. Nucl. Med.* **49** 1875–83

Hofmann M *et al* 2011 MRI-based attenuation correction for whole-body PET/MRI: quantitative evaluation of segmentation and Atlas-based methods *J. Nucl. Med.* **52** 1392–9

Hu Z *et al* 2009 MR-based attenuation correction for a whole-body sequential PET/MR system *IEEE Nuclear Science Symp. & Medical Imaging Conf. (Orlando, FL, USA, 25–31 October 2009)* pp 3508–12

Izquierdo-Garcia D *et al* 2014 An SPM8-based approach for attenuation correction combining segmentation and nonrigid template formation: application to simultaneous PET/MR brain imaging *J. Nucl. Med.* **55** 1825–30

Johansson A, Karlsson M and Nyholm T 2011 CT substitute derived from MRI sequences with ultrashort echo time *Med. Phys.* **38** 2708–14

Jonsson J H *et al* 2015 Accuracy of inverse treatment planning on substitute CT images derived from MR data for brain lesions *Radiat. Oncol.* **10** 13

Jonsson J H, Johansson A, Soderstrom K, Asklund T and Nyholm T 2013 Treatment planning of intracranial targets on MRI derived substitute CT data *Radiother. Oncol.* **108** 118–22

Kapanen M and Tenhunen M 2013 *T*1/*T*2*-weighted MRI provides clinically relevant pseudo-CT density data for the pelvic bones in MRI-only based radiotherapy treatment planning *Acta Oncol* **52** 612–8
Keereman V *et al* 2010 MRI-based attenuation correction for PET/MRI using ultrashort echo time sequences *J. Nucl. Med.* **51** 812–8
Kim J *et al* 2015 Implementation of a novel algorithm for generating synthetic CT images from magnetic resonance imaging data sets for prostate cancer radiation therapy *Int. J. Radiat. Oncol. Biol. Phys.* **91** 39–47
Klein S, Staring M, Murphy K, Viergever M A and Pluim J P W 2010 Elastix: a toolbox for intensity-based medical image registration *IEEE Trans. Med. Imaging* **29** 196–205
Kovesi P 2000 Phase congruency: a low-level image invariant *Psychol. Res.* **64** 136–48
Lotjonen J M *et al* 2010 Fast and robust multi-atlas segmentation of brain magnetic resonance images *Neuroimage* **49** 2352–65
Low D A, Harms W B, Mutic S and Purdy J A 1998 A technique for the quantitative evaluation of dose distributions *Med. Phys.* **25** 656–61
Marshall H R *et al* 2013 Description and assessment of a registration-based approach to include bones for attenuation correction of whole-body PET/MRI *Med. Phys.* **40** 082509
Martinez-Moller A *et al* 2009 Tissue classification as a potential approach for attenuation correction in whole-body PET/MRI: evaluation with PET/CT data *J. Nucl. Med.* **50** 520–6
McAuliffe M J *et al* 2001 Medical image processing, analysis and visualization in clinical research *Proc. 14th IEEE Symp. on Computer-Based Medical Systems* pp 381–6
Mehranian A, Arabi H and Zaidi H 2016 Vision 20/20: magnetic resonance imaging-guided attenuation correction in PET/MRI: challenges, solutions, and opportunities *Med. Phys.* **43** 1130–55
Mehranian A and Zaidi H 2015 Joint estimation of activity and attenuation in whole-body TOF PET/MRI using constrained Gaussian mixture models *IEEE Trans. Med. Imaging* **34** 1808–21
Noorda Y H *et al* 2014 Registration of CT to pre-treatment MRI for planning of MR-HIFU ablation treatment of painful bone metastases *Phys. Med. Biol.* **59** 4167–79
Nyholm T, Nyberg M, Karlsson M G and Karlsson M 2009 Systematisation of spatial uncertainties for comparison between a MR and a CT-based radiotherapy workflow for prostate treatments *Radiat. Oncol.* **4** 54
Ortiz C G and Martel A L 2012 Automatic atlas-based segmentation of the breast in MRI for 3D breast volume computation *Med. Phys.* **39** 5835–48
Paulus D H, Oehmigen M, Gruneisen J, Umutlu L and Quick H H 2016 Whole-body hybrid imaging concept for the integration of PET/MR into radiation therapy treatment planning *Phys. Med. Biol.* **61** 3504–20
Paulus D H *et al* 2015 Whole-body PET/MR imaging: quantitative evaluation of a novel model-based MR attenuation correction method including bone *J. Nucl. Med.* **57** 1061–6
Prabhakar R *et al* 2007 Comparison of computed tomography and magnetic resonance based target volume in brain tumors *J. Cancer Res. Ther.* **3** 121–3
Rank C M *et al* 2013 MRI-based treatment plan simulation and adaptation for ion radiotherapy using a classification-based approach *Radiat. Oncol.* **8** 51
Rasch C, Steenbakkers R and van Herk M 2005 Target definition in prostate, head, and neck *Semin. Radiat. Oncol.* **15** 136–45
Rezaei A *et al* 2012 Simultaneous reconstruction of activity and attenuation in time-of-flight PET *IEEE Trans. Med. Imaging* **31** 2224–33
Schmidt M A and Payne G S 2015 Radiotherapy planning using MRI *Phys. Med. Biol.* **60** R323–61
Sjölund J, Forsberg D, Andersson M and Knutsson H 2015 Generating patient specific pseudo-CT of the head from MR using atlas-based regression *Phys. Med. Biol.* **60** 825–39
Tustison N J *et al* 2010 N4ITK: improved N3 bias correction *IEEE Trans. Med. Imaging* **29** 1310–20
Uh J, Merchant T E, Li Y, Li X and Hua C 2014 MRI-based treatment planning with pseudo CT generated through atlas registration *Med. Phys.* **41** 051711–8
Ulin K, Urie M M and Cherlow J M 2010 Results of a multi-institutional benchmark test for cranial CT/MR image registration *Int. J. Radiat. Oncol. Biol. Phys.* **77** 1584–9
Yushkevich P A *et al* 2006 User-guided 3D active contour segmentation of anatomical structures: significantly improved efficiency and reliability *Neuroimage* **31** 1116–28
Zaidi H *et al* 2011 Design and performance evaluation of a whole-body Ingenuity TF PET-MRI system *Phys. Med. Biol.* **56** 3091–106
Zhuang X and Shen J 2016 Multi-scale patch and multi-modality atlases for whole heart segmentation of MRI *Med. Image Anal.* **31** 77–87